In-Situ Two- and Three-Phase Saturation Monitoring Using Dual-Resonance ^{1}H/^{23}Na MRI During Coreflooding

Daan W. de Kort[1,*], *Efraïm C.* Keijzer[1], *Matthias* Appel[2], *Benjamin C.* Anger[2] and *Tibi G.* Sorop[1]

[1]Shell Global Solutions Intl B.V., Grasweg 31, 1031 HW, Amsterdam, The Netherlands
[2]Shell Intl Exploration and Production Inc., 3333 Highway 6 South, Houston, TX 77082, USA

Abstract. Coreflooding experiments with in-situ saturation monitoring (ISSM) are essential for determining key reservoir parameters, including relative permeability, trapped gas saturations, and remaining oil saturations. This study demonstrates the application of NMR and MRI to monitor two- and, for the first time, three-phase saturations in situ during unsteady-state coreflooding—directly applicable to gas injection, water-alternating-gas (WAG), and CCS workflows. A calibration-based correction strategy was implemented to ensure quantitative accuracy of saturation profiles, addressing a known limitation of MRI-based ISSM. Validation was achieved through mass balance checks and history-matched numerical simulation. Two experimental applications demonstrate the utility of this approach. The first employs a proton–sodium dual-resonance NMR probe for direct, in situ quantification of brine and oil saturations during three-phase flow, with the third phase inferred by difference—representing a novel application of MRI for three-phase monitoring. The second uses proton NMR to monitor brine imbibition into a supercritical CO_2-saturated rock, exploiting natural contrast to visualise the displacement front and quantify trapped gas. This required careful control due to the strong sensitivity of CO_2 properties to fluctuations in pressure and temperature. These results demonstrate the potential of MRI-based ISSM to advance understanding of multiphase transport in both enhanced recovery and CO_2 storage.

1 Introduction

Coreflooding experiments are aimed at quantifying the mobility of pore fluids under multi-phase flow conditions. Fluid displacement efficiencies can be derived by monitoring the volumes of injected and produced fluids. The experiments are aimed at determining input parameters for reservoir simulation, formation evaluation, well tests and interventions. Parameters such as end-point relative permeabilities and saturations can be determined, or full relative permeability curves can be inferred [1,2]. Fluids injected during the experiments are typically liquid hydrocarbons, brine, and polymer or surfactant solutions, but can also be gaseous hydrocarbon or CO_2. For instance, injecting CO_2 into a brine saturated rock would be representative of drainage processes in the subsurface that are relevant for carbon capture and storage (CCS) applications.

To account for the effects of capillarity during the experiment, it is necessary to obtain the spatial distribution of the different pore fluids as a function of position along the core and of time. Measurement of the distribution of pore fluids along the length of the core as function of space and time is referred to as in situ saturation monitoring (ISSM). Primarily, ISSM provides a direct measurement of the amount of fluid inside of the core, instead of indirectly via measurement of injected volumes and downstream collection of produced fluids. Secondarily, ISSM provides important insight into the extent of the capillary end-effect, which causes non-uniform saturations along the length of the rock sample. The capillary end-effect is caused by the discontinuity in capillary pressure for the wetting phase at the outlet face of the sample [3]. The resulting non-uniform saturation distribution—an unavoidable artefact of laboratory-scale experiments—can lead to deviations in relative permeability curves when using mass balance-derived ‘effective’ saturation values. Due to the finite length of core plugs, the capillary end-effect can be significant. In this context, ISSM provides a valuable constraint, enhancing the interpretation of coreflooding data and the derivation of more accurate relative permeability relationships.

In situ saturation monitoring (ISSM) using imaging techniques enables direct observation of the capillary end-effect, allowing it to be properly accounted for through analytical corrections [4] or inverse modelling (i.e., history-matching of numerical flow simulations).

The most widely used ISSM techniques rely on X-ray or gamma-ray attenuation measurements, from which relative fluid saturations are inferred through calibration under well-defined saturation conditions. X-rays are particularly favoured due to their linear attenuation response, which facilitates straightforward conversion to saturation values [5]. Although the contrast between two fluid phases is low compared to the attenuation by the

---

[*] Corresponding author: daan.dekort@shell.com

rock matrix, the signal-to-noise ratio is typically sufficient to distinguish between phases—especially when a contrast agent is introduced to enhance attenuation in one of the fluids.

In this paper, we present recent developments and applications of time-lapse, spatially-resolved nuclear magnetic resonance (NMR)—commonly referred to as magnetic resonance imaging (MRI)—for in situ saturation monitoring during corefl ooding experiments. Unlike attenuation-based methods, MRI offers direct fluid phase discrimination via chemical or nuclear contrast—particularly useful when one fluid phase is NMR-invisible, such as gas. While NMR is widely established in petrophysical analysis, the systematic use of spatially-resolved NMR/MRI in coreflooding studies [6–11], particularly for deriving multiphase flow properties such as relative permeability curves, represents an emerging and evolving area of research [12–19].

This work has three primary objectives. First, to validate MRI as a reliable method for ISSM for two-phase flow, achieved by comparing MRI-derived saturation changes with independently measured mass balance during coreflooding. Also, through inverse modelling, we show that the interpretation of the experiment in terms of relative permeability and capillary pressure curves is plausible. Second, to establish a proof of principle for three-phase ISSM using a dual-resonance proton-sodium NMR probe, enabling simultaneous quantification of a brine and oil phase, with sodium providing a brine-specific signal. The third phase—characterised by negligible NMR signal, such as, for instance, a gas—is inferred by difference. Third, to illustrate that coreflooding with MRI-based ISSM produces meaningful results in the challenging case of the presence of a gas phase, through an example involving supercritical CO_2.

There are several reasons why this demonstration is necessary. NMR inherently detects fluids, offering the potential for phase contrast without the need for contrast agents—unlike X-ray-based methods. However, this advantage has so far been limited to specific rock–fluid systems that naturally lend themselves to phase-selective NMR measurements. Known strategies for selectively imaging a single phase in two-phase systems without contrast agents include exploiting chemical shift differences [20] or relaxation time contrasts [21]. Yet, these approaches are often impractical for complex reservoir oils or low-permeability rocks. Another strategy involves substituting one of the phases with a model fluid that is NMR-invisible, such as deuterated water (D_2O) or perfluorinated oils. While effective, these substitutes may not accurately replicate the properties of in-situ fluids, thereby diminishing the comparative advantage of NMR over X-ray methods.

In the context of two-phase flow, interest in NMR is growing—particularly for experiments involving CO_2. Since proton NMR is the most commonly used modality and CO_2 is invisible to it, inherent phase contrast is achieved. However, this also necessitates the development of robust calibration and measurement protocols to ensure that saturation estimates are quantitative and that the results can be reliably interpreted in terms of relative permeability, using frameworks such as inverse modelling.

For three-phase flow, MRI provides a unique capability for in situ saturation monitoring due to its ability to detect multiple nuclei simultaneously, with each nucleus corresponding to a specific phase or subset of phases. We propose that this approach can be applied to three-phase ISSM involving a gas and two immiscible liquids (e.g., brine and oil), which is particularly relevant for scenarios such as live crude mobility studies or water-alternating-gas (WAG) injection schemes. The introduction of an additional degree of freedom in three-phase flow systems, relative to two-phase flow, necessitates a corresponding independent measurement to fully resolve phase distributions. Multinuclear NMR, which enables the simultaneous detection of signals from multiple nuclear species using a single probe, offers a viable approach to obtaining this complementary information. Quantitative non-proton NMR measurements—such as those using sodium and carbon—have been described in the literature [22,23] and applied during coreflooding experiments [17], but have not yet been used for in situ saturation monitoring under three-phase flow conditions.

1.1 Sensitivity and relaxation in NMR

To establish a robust calibration protocol that allows accurate measurement of fluid saturations by NMR/MRI, it is necessary to understand two main factors that affect the NMR signal: the sensitivity of the measurement, and the relaxation dynamics of the NMR signal. These elements will be discussed in more detail in the following sections.

1.1.1 Sensitivity: nuclei and magnetic field strength

Detection in NMR relies on the absorption and emission of radiofrequency (RF) waves by atomic nuclei with a nonzero magnetic moment placed inside an external magnetic field. NMR sensitivity is primarily determined by the detected nucleus and the strength of the magnetic field. In particular, the signal-to-noise ratio (SNR) of an NMR measurement is given by: $SNR \propto n\gamma^{5/2}B_0^{3/2}m^{1/2}$, where n is the number of nuclei present in a sample, γ the gyromagnetic ratio of the nucleus, B_0 the magnetic field strength, and m the number of acquired signal averages.

Estimates of relative NMR sensitivity for three widely studied nuclei—^{1}H, ^{23}Na, and ^{13}C—at natural isotopic abundance, all of which are commonly present in the fluids used in coreflooding experiments, are presented in Table 1. By far the most frequently utilised nucleus in magnetic resonance methods is the proton (^{1}H), owing to the ubiquity of hydrogen atoms in many materials and its high NMR sensitivity. The latter is due to the high natural abundance of the NMR active nuclear isotope ^{1}H and its high gyromagnetic ratio. Carbon atoms are also abundant in many materials, but its NMR sensitivity is very low compared to protons, primarily due to the low natural abundance of isotope ^{13}C. Sodium atoms are relatively scarce in most materials, but due to the moderate NMR sensitivity of ^{23}Na, detection is straightforward when present in sufficient concentrations, such as in brine.

Furthermore, NMR sensitivity is linearly proportional to the number of nuclei n within the detection volume, and also scales with the strength of the external magnetic field as $B_0^{3/2}$. In rock core analysis laboratories, typical magnetic field strengths range from approximately 0.05 T for benchtop permanent magnet systems to around 2 T for superconducting magnet systems. This corresponds to an approximate sensitivity difference of a factor of ~250. In practical terms, permanent magnet NMR systems are generally limited to proton NMR, whereas non-proton NMR typically requires the higher sensitivity afforded by superconducting NMR systems.

Table 1. Relative NMR sensitivity to hydrogen, sodium and carbon at natural isotopic abundance.

Nuclear isotope	^{1}H	^{23}Na	^{13}C
Natural abundance of nuclear isotope [%]	99.99	100	1.07
Gyromagnetic ratio γ [MHz/T]	42.6	11.3	10.7
SNR vs. hydrogen at equal nuclei count	1	3.6×10^{-2}	3.4×10^{-4}
Signal averages m needed to match hydrogen SNR	1	8×10^{2}	9×10^{6}

1.1.2 Relaxation: T_1, T_2, and signal decay

Apart from sensitivity, relaxation is a key concept that can affect the quantitative nature of saturation measurements. In MRI, contrast is generated by applying a sequence of short RF and magnetic field gradient pulses. This sequence manipulates the net magnetisation of the sample, which is then detected as an RF signal. After excitation, the magnetisation relaxes back to equilibrium, characterised by two key times: T_1 (longitudinal relaxation) and T_2 (transverse relaxation).

The mechanisms behind T_1 and T_2 depend on the nuclear spin. For spin-½ nuclei like ^{1}H, dipolar interactions dominate. For spin-$^3/_2$ nuclei like ^{23}Na, stronger quadrupolar interactions—sensitive to electric field gradients—lead to faster relaxation.

To detect a signal, the magnetisation must be rotated into the transverse plane, where it decays due to spin dephasing (T_2). T_2 is especially influenced by molecular mobility: lower mobility (e.g., in small pores or viscous fluids) shortens T_2. In porous media, ^{1}H T_2 often reflects pore size, but this link is less direct for quadrupolar nuclei like ^{23}Na [24]. Paramagnetic species (e.g., iron oxides) also accelerate relaxation. In solids, T_2 is orders of magnitude shorter than in liquids.

1.2 Implications for quantitative ISSM and pulse sequence optimisation

Quantitative MRI imaging of fluid saturations depends critically on both nuclear sensitivity and relaxation dynamics. Sensitivity–determined by the nucleus type and its concentration—sets the upper limit of detectable signal. However, T_1 and T_2 relaxation during the pulse sequence leads to signal loss, especially when relaxation times are short relative to the sequence duration. This relaxation behaviour has multiple implications: on one hand, it is beneficial in that it naturally suppresses signal from the solid matrix, which is not of interest in fluid saturation studies. However, it also reduces signal from fluids with short T_2 values, such as those in small pores or with high viscosity, potentially compromising quantitative accuracy. Notably, shorter T_1 relaxation times offer a practical advantage by enabling faster signal averaging. This is particularly beneficial for nuclei such as ^{23}Na, which typically exhibit short T_1 values. While higher magnetic fields improve sensitivity, they also increase internal magnetic field gradients due to susceptibility differences between rock and fluid. These gradients, combined with molecular diffusion, further shorten T_2 and reduce signal. Thus, the feasibility of an MRI experiment is constrained by sensitivity and relaxation-induced signal decay, which together limit the amount and complexity of spatial or molecular information that can be encoded with the available relaxation time window.

To address these challenges, pulse sequence selection and optimisation is key. Green et al. [25–28] demonstrated robust one-dimensional profiling of fluid saturations in rocks using MRI following centrifuge drainage experiments. For time-lapse imaging during coreflooding, the spin-echo single point imaging (SE-SPI) sequence is often preferred for its robustness and for its ability to provide well defined spatial profiles with minimal distortion from relaxation effects [29,30]. It uses a single excitation, spatial encoding, and refocusing pulse to acquire one echo per profile point, minimising delays that would otherwise lead to signal loss.

Despite hardware optimisation, some signal loss is inevitable—especially for components with short T_2—and must be corrected. This study applied an offset correction by comparing SE-SPI saturation profiles to bulk saturation measurements using the Carr-Purcell-Meiboom-Gill (CPMG) experiment, which is the gold standard for pore volume measurements with NMR [31,32]. The difference in total signal intensity provides an offset correction, uniformly applied across the profile to restore quantitative accuracy. This correction approach remains valid provided that the extent of signal loss does not exceed the volume of immobile water present in the pore space.

1.3 Scope of this study

This study evaluates the performance of MRI for in situ saturation monitoring (ISSM). Building on the previous discussion of factors affecting quantitative accuracy and the proposed offset correction strategy, the following experiments serve as demonstration cases.

The first set of experiments demonstrates two- and three-phase ISSM during unsteady-state drainage coreflooding. A brine-saturated rock sample is drained by a perfluorinated oil, which contains neither protons nor sodium and is therefore invisible to both ^{1}H and ^{23}Na MRI. This selective visibility enables direct observation of the brine phase. Quantitative accuracy is assessed by comparing MRI signal changes to mass balance calculations, and by verifying that the signal changes in ^{1}H and ^{23}Na MRI are equivalent. Additionally, inverse modelling is used to ensure that the results are interpretable in terms of relative permeability curves.

The final experiment illustrates MRI-based monitoring of coreflooding in the presence of a gas phase (supercritical CO_2), specifically during imbibition into a rock sample previously drained to connate water saturation. This establishes the applicability of MRI to coreflooding experiments involving compressible non-wetting phases, which is essential for studies using any live reservoir fluid. Accurate control of gas flow is critical in such experiments. Furthermore, the ability to quantify residual/trapped CO_2 saturation (S_{grw}) is particularly relevant for carbon capture and storage (CCS) applications [33].

This paper is structured as follows. In Section 2, the NMR apparatus and coreflooding systems used in this study are described, as well as the relevant details of the coreflooding experiments. In Section 3, the experimental results are presented, focusing on establishing the quantitative accuracy of the experiments and their interpretation.

2 Setup and data acquisition

2.1. Integrated coreflooding/MRI setups

Two coreflooding setups were designed and constructed for the injection of live fluids at temperatures and pressures under which the same phase behaviour phenomena observed in reservoir fluids can be reproduced. System temperature can be controlled between room temperature and 100°C. Various pressure readings can be logged during fluid injection, enabling the measurement of pressure drop across the core. Additionally, injected and produced fluids can be monitored quantitatively with high-accuracy pumps.

Each coreflooding setup is coupled to NMR/MRI imaging systems equipped with a core holder/pressure cell made of non-metallic materials, ensuring no interference with the RF probe. The core holder sits within the RF probe inside the magnet.

2.1.1 Monitoring and control of experimental conditions

Pressure differentials were recorded via a differential pressure gauge across the core sample. Due to the presence of the bulky NMR magnet, the pressure taps were placed above and below the core holder, outside of the magnet.

During all experiments, a confining pressure of 15–20 bar higher than the pore pressure was maintained. Perfluorinated oil (Fluorinert FC-3283, 3M) was used as the confining fluid, as it is invisible to both ^{1}H and ^{23}Na NMR. The sample temperature is maintained via thermal contact with the recirculated confining fluid, which flowed through the annulus of the core holder.

Injection and production volumes were recorded via positive displacement pumps (Vindum VP series) on the injection and production end of the sample. Direct collection/sampling of produced volumes was challenging due to the large dead volumes relative to the sample pore volume on the live fluid injection systems, or for a live fluid experiment.

2.1.2 ^{1}H MRI on permanent magnet system

The first coreflooding unit was integrated with an Oxford Instruments (UK) 0.30 T GeoSpec2+ permanent-magnet 3D MRI system. This setup incorporates an Oxford Instruments P5 overburden cell, capable of withstanding pressures up to 2,500 psi (172 bar). The P5 cell serves as a core holder and features an integrated ^{1}H RF probe, operating at a resonance frequency of 12.8 MHz.

2.1.3 ^{1}H/^{23}Na dual-resonance MRI on superconducting magnet system

The second coreflooding unit was connected to an MR Solutions (UK) ImaCore variable field, vertical-bore, superconducting 3D MRI system. For this study, the magnetic field strength was held at 2.12 T.

A ^{1}H/^{23}Na dual-resonance quadrature RF probe and preamplifier were designed and constructed by MRF Innovations Ltd (UK), enabling quadrature detection on both frequencies for enhanced sensitivity. At 2.12 T, the resonance frequencies are 90.5 MHz for ^{1}H, and 23.9 MHz for ^{23}Na. The data acquisition software was modified to allow programmable switching between the two frequencies during operation.

A ceramic core holder (Daedalus Innovations LLC, USA) rated for pressures up to 6,000 psi (414 bar) was placed within the RF probe.

2.2 Rock samples and experimental protocol

In Table 2, the basic properties of the three samples used in this study are summarised and Table 3 shows the experiments performed on each of the samples.

2.2.1 Drainage experiments

In experiments A and B, unsteady-state drainage corefloods were carried out by initially saturating the rock samples with brine. A perfluorinated oil was then injected at an initial, baseline flow rate Q of 0.03 ml/min, corresponding to a Darcy (superficial) velocity of 0.06 mm/min, until the injection pressure and saturation reached a steady state. This was followed by sequential bump floods at elevated flow rates of 0.3 and 3 ml/min (0.6 and 6 mm/min, respectively) to induce pressure transients and enhance the interpretation of the flow dynamics. In experiment A, Fluorinert FC-3283 (3M) was used as the perfluorinated oil, while Galden SV 110 (Syensqo) was used in experiment B. The rock sample is oriented vertically inside the imaging system, and the perfluorinated oil is injected from bottom to top because of its higher density. During the experiments, a back pressure of 6 bar was maintained. Additionally, in experiment B, proton-bearing *n*-decane—immiscible with both the brine and perfluorinated oil—was subsequently injected at 0.03 ml/min (0.06 mm/min), to demonstrate three-phase ISSM. This approach highlights the characteristic immiscibility of perfluorinated oils with both aqueous and hydrocarbon phases.

Table 2. Physical properties of rock samples and fluids used in experiments A, B, and C. Fluid properties are reported at the experimental temperature and backpressure conditions.

Property	**Unit**	**Exp. A**	**Exp. B**	**Exp. C**
rock type	—	Berea sandstone	Berea sand-stone	sand-stone
k_{brine}	mD	37	104	7.1
porosity ϕ	%	20.3	20.6	12.3
⌀ area A	cm^2	4.95	5.15	5.23
length L	cm	4.02	5.01	3.73
non-wetting phase	—	Fluorinert	Galden	CO_2
η_{nw}	mPa·s	1.4	1.32	0.03
ϱ_{nw}	kg/m^3	1.8	1.71	0.58
η_{brine}	mPa·s	1.07	1.53	0.65
ϱ_{brine}	kg/m^3	1.03	1.15	1.13
[Na]	mol/L	0.5	2.8	3.5
temperature	°C	25	25	50
backpressure	bar	6	6	100

Table 3. Overview of experiments presented in this paper.

Exp.	**Field Strength; Nuclei; ISSM type**	**Experimental description**
A	0.30 T ^{1}H Two-Phase ISSM	Unsteady-state **drainage** with perfluorinated oil
B	2.12 T ^{23}Na/ ^{1}H (dual) Three-Phase ISSM	Unsteady-state **drainage** with perfluorinated oil followed by *n*-decane injection
C	0.30 T ^{1}H Two-Phase ISSM	Unsteady-state **imbibition** of brine into sample at S_{wc}, saturated with supercritical CO_2

2.2.2 Imbibition experiment

In experiment C, the imbibition procedure was carried out as follows. The rock sample was first saturated with brine and then drained using a centrifuge against air. A centrifuge was chosen for drainage because it results in a lower residual brine saturation than coreflooding with (supercritical/dense phase) CO_2 at experimentally manageable flow rates. Once completed, the sample was mounted in the core holder, where the remaining air was displaced by CO_2. The system was then brought to a pressure of 100 bar and a temperature of 50 °C. Brine was subsequently re-imbibed into the sample, displacing CO_2 at a baseline flow rate of 0.02 ml/min (0.04 mm/min), followed by a series of bump floods.

2.3 MRI saturation profiling experiments

The NMR acquisition protocol is based on a quantitative bulk measurement of pore volume using the conventional CPMG experiment, which is routinely employed for this purpose. To obtain spatially resolved information, the spin-echo single-point imaging (SE-SPI) experiment is used to generate an intensity profile that reflects the local liquid content at each spatial position. As described earlier, signal losses due to T_2 relaxation during the spatial encoding period are corrected post-acquisition using an offset adjustment. This correction is determined by comparing the total signal intensity from the SE-SPI and CPMG measurements on a fully brine-saturated sample ($S_w = 1$). Minor background signals originating from the RF probe or core holder are also accounted for. After these corrections, all intensity profiles are normalised to a reference profile acquired at $S_w = 1$.

In the two-phase experiments, which use ^{1}H NMR and involve one NMR-invisible phase, the corrected profiles directly reflect local brine saturation. The number of spatial positions and signal averages is selected to keep the acquisition time for each saturation profile around 5 minutes, with a spatial resolution of approximately 1.5 mm.

In the three-phase experiments, successive ^{1}H and ^{23}Na saturation profiles are acquired. The number of spatial positions and acquisition time are kept consistent between the two nuclei to enable direct comparison and combination of the signal for three-phase saturation calculations. As a result, the ^{1}H profiles exhibit a higher SNR than the ^{23}Na profiles.

Table 4 lists key NMR acquisition parameters that affect measurement accuracy. The superconducting NMR system provides better signal sensitivity due to the stronger magnetic field, but it also requires longer 180° RF pulses. These pulses—used to flip the magnetisation in spin-echo sequences—reflect how efficiently the probe delivers RF energy. Longer pulses are common at higher fields, not because of any limitation in a specific probe, but due to the higher operating frequencies and the engineering trade-offs involved in high-field probe design. These longer pulses limit how short the echo times can be in CPMG and SE-SPI sequences, which can reduce accuracy for fast-relaxing signals. This highlights the need to consider both field strength and RF performance when comparing NMR systems.

Table 4. NMR parameters showing resonance frequencies, RF pulse durations, and echo times.

System	**Nu-cleus**	**NMR fre-quency** [MHz]	**180° RF pulse length** [µs]	**CPMG echo time** [µs]	**SE-SPI echo time** [µs]
0.30 T; ^{1}H RF probe	^{1}H	12.8	21	128	600
2.12 T; ^{1}H/^{23}Na RF probe	^{1}H	90.5	74	422	700
	^{23}Na	23.9	55	402	700

3 Results and discussion

3.1 Experiment A: Two-phase ISSM using ^{1}H NMR, and inverse modelling

The results of the unsteady-state drainage coreflood experiment, along with their interpretation via inverse modelling, are presented in Figs 1–5. The discussion begins with the experimental observations, followed by a description of the numerical simulation used to infer relative permeability curves from the measured data.

Fig. 1 displays the saturation profiles, which have been offset-corrected and normalised as previously described. The profiles are truncated at the inlet due to observed inflow artefacts. The data capture the initial advance of the flood front and a progressive decrease in brine saturation over time. Two bump floods were performed, further reducing the brine saturation. A pronounced capillary end-effect is evident near the outlet, characteristic of the forced drainage process during oil injection.

Fig. 2 shows the pressure drop across the core as a function of time. A correction was applied to account for the gravity head buildup during the initial injection of perfluorinated oil, which has a high mass density. The pressure increase associated with the two bump floods is clearly visible.

Fig. 3 presents the production data, which were derived directly from the full saturation profiles (without truncation).

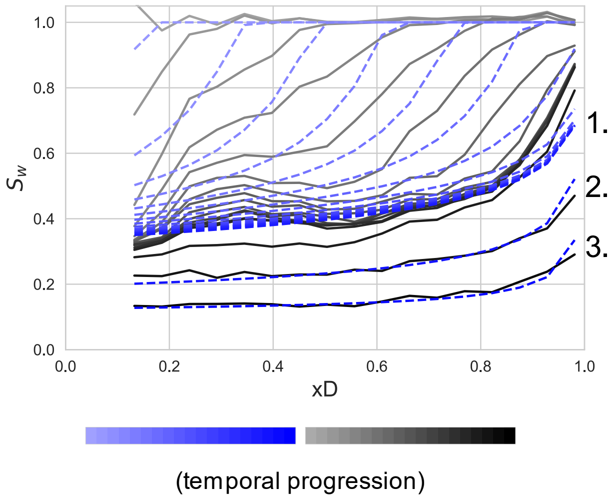

Fig. 1. Water saturation profiles as function of fractional position xD along the core plug, from experiment (–) and simulation (- -). Flow direction of perfluorinated oil from left to right. Saturations become successively lower with time. Points 1, 2 and 3 indicate the end of the initial injection step and the subsequent two bump floods, corresponding to the times at which saturation profiles were stable.

3.1.1 Inverse modelling

Numerical simulations were performed by solving the coupled mass balance equations and Darcy's law for one-dimensional, two-phase, immiscible, and incompressible flow through porous media. This modelling framework, commonly employed in both coreflooding and reservoir-scale studies, incorporated experimentally representative boundary conditions, including a gravitational term to account for fluid density contrasts. Capillary pressure between the two phases was included as a dynamic, saturation-dependent function. Together with the relative permeability curves, this capillary pressure relationship was treated as an adjustable parameter set. History matching was performed against measured saturation profiles, produced fluid volumes, and pressure data, with iterative refinement of these constitutive relationships to reproduce key experimental observations, including the capillary end-effect.

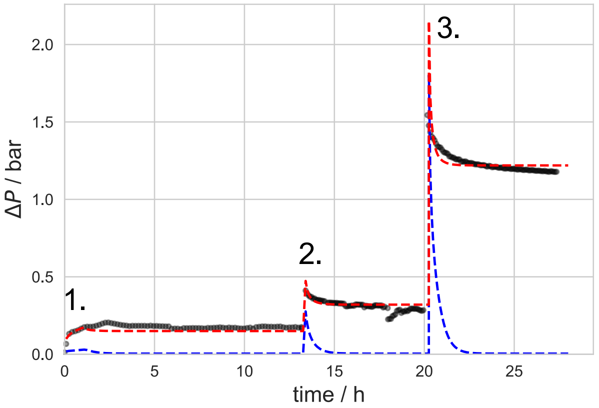

Fig. 2. Pressure drop ΔP measured across the rock sample during the coreflood (●); simulated oil (- -) and brine (- -) ΔP. Time points 1, 2 and 3 mark the onset of the initial injection step and the subsequent two bump floods, respectively.

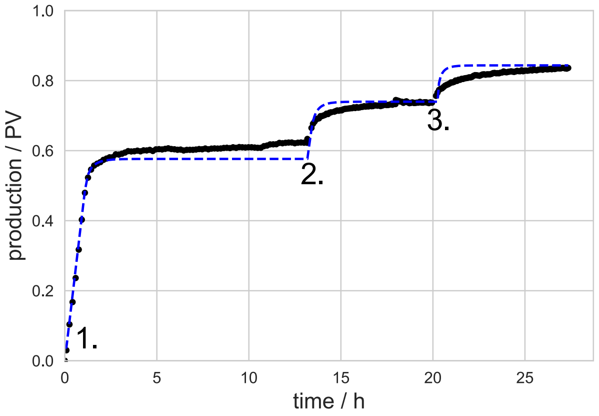

Fig. 3. Produced volume of brine (●) from the rock sample as a function of time; simulation (- -). Time points 1, 2 and 3 mark the onset of the initial injection step and the subsequent two bump floods, respectively.

The open-source Python package *Core2Relperm* [34] was used to carry out the inverse modelling procedure described above. It employs LET-type functions [35] to represent relative permeability and uses the Skjæveland formulation [36] for the capillary pressure curve. While these parameterisations may impose constraints on the solution space, their integration within a minimisation-based history-matching framework grants access to the Jacobian matrix. This enables computation of the parameter covariance matrix, which can be used to quantify uncertainty margins via Monte Carlo sampling. Such uncertainty quantification is particularly important for unsteady-state corefloods, where the inferred relative permeability and capillary pressure curves are often subject to significant uncertainty. Although manual history matching may yield a closer fit, the use of parameterised functions within an optimisation framework provides a systematic and reproducible means of assessing confidence intervals on the derived flow functions.

For this experiment, the measured pressure drop was interpreted as the oil-phase pressure drop, since the injected fractional flow of brine was zero and, for most of the experiment, only the oil phase was mobile. As the experiment represents a drainage process initiated from a fully brine-saturated core, the residual oil saturation was set to zero. The history match to the experimental data is shown in Figs 1–3, while the resulting relative permeability and drainage capillary pressure curves—along with their associated uncertainty estimates—are shown in Figs 4 and 5.

A good history match was achieved for the pressure drop data, and a reasonable match for the production data, although some deviations were observed during the initial desaturation phase. For the saturation profiles, a balance was struck between matching the profiles during flood front passage and the more stable profiles observed at the end of each flow rate step. While the profiles acquired during flood front passage theoretically contain valuable information about relative permeability in the higher water saturation (S_w) range, they also exhibit artefacts between positions xD = 0.25–0.5, and are affected by motional blurring due to the finite acquisition time of each profile (5 minutes) [37]. As a result, these profiles may be less reliable than the stable end-point profiles. Additionally, the minimisation algorithm assigns equal weight to all profiles, including those acquired during flood front passage and the three end-point profiles for each flow rate step. This introduces ambiguity into the optimisation process. However, it was verified that excluding the flood front profiles from the history match leads to a quantitatively improved fit to the production data and the remaining saturation profiles. Importantly, however, this exclusion had no significant impact—within the estimated error margins—on the inferred relative permeability and capillary pressure curves.

Regarding the relative permeability curves in Fig. 4, the uncertainty margins reflect the numerical uncertainty associated with the best-fit history match. However, they do not capture potential model limitations arising from the use of the LET and Skjæveland parameterisations. Notably, the inferred oil relative permeability at connate water saturation is significantly greater than 1—despite a wide uncertainty band. This may be attributed to differing slip boundary conditions of the perfluorinated oil compared to the brine phase. This observation is supported by a measurement of the effective relative permeability to the perfluorinated oil conducted at the end of the test, as well as by the fact that the Klinkenberg permeability of this rock sample is similarly higher than its brine permeability—a trend commonly observed, particularly in clay-rich rocks.

Fig. 5 presents the matched capillary pressure curve, which represents the capillary pressure required to reproduce the observed capillary end-effect. While capillary pressure plays a limited role in reservoir-scale displacement processes, it is critical for interpreting plug-scale coreflooding behaviour. Uniquely for a drainage coreflood, the numerically derived capillary pressure curve can be compared to an experimentally measured drainage capillary pressure curve. However, discrepancies are observed when comparing the matched capillary pressure curve to the mercury intrusion capillary pressure (MICP) result, which was transformed to reflect the experimental fluid system (perfluorinated oil/brine) using the Leverett-*J* function. The poor scaling outcome suggests that fluid-specific interfacial tension and wettability differences, not captured by standard Leverett-*J* scaling, affect capillary entry pressures and curve shape. Additional sources of error may include sample-to-sample heterogeneity—since the MICP was performed on a different plug from the same outcrop—as well as uncertainties related to clay-bound water corrections, closure effects, and the translation of MICP pressures to equivalent values for the oil–brine system using interfacial properties. Given these factors, a perfect match should not be expected.

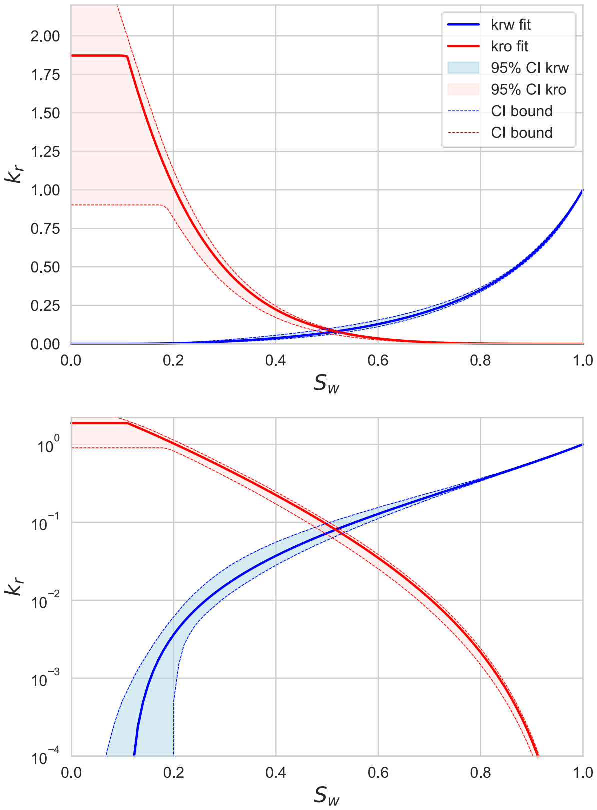

Fig. 4. Relative permeability curves (on linear and logarithmic scales) inferred through inverse modelling of the experimental data. CI is the 3σ confidence interval.

3.1.2 Benchmarking experimental accuracy of saturation measurements

Since it was not possible to directly sample the produced brine volumes as an independent benchmark for validating the NMR-derived saturation measurements, an alternative approach was employed to assess measurement accuracy. During the initial stage of the coreflood—prior to the breakthrough of the perfluorinated oil flood front—the volume of injected oil should correspond to the average desaturation inferred from the NMR saturation profiles. The cross plot shown in Fig. 6 confirms this agreement, indicating that the saturation measurements are accurate and that the applied offset correction was of the right magnitude. This validation supports the conclusion that the experiment is both quantitatively accurate and interpretable in terms of relative permeability.

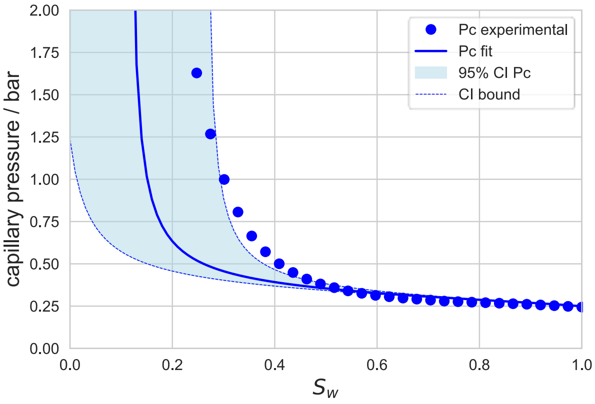

Fig. 5. Drainage capillary pressure curve inferred through inverse modelling of the experimental data. CI is the 3σ confidence interval. The dotted data are the MICP-derived capillary pressure curve, converted to the relevant fluid pair through a Leverett-*J* transformation. The vertical axis is limited to the maximum pressure drop seen during the experiment.

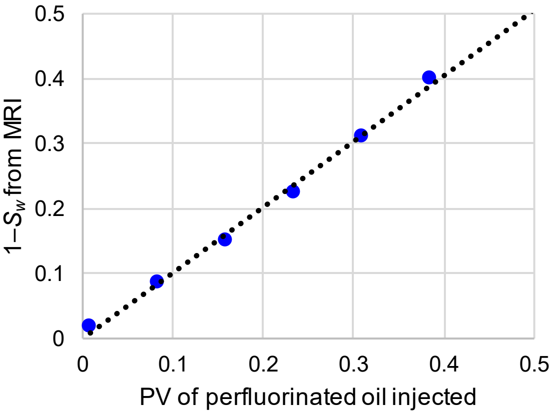

Fig. 6. Comparison of the desaturation seen in the MRI experiment versus the number of pore volumes of perfluorinated oil injected prior to breakthrough of the flood front. For reference, the dotted line is the 1:1 identity.

3.2 Experiment B: Three-phase ISSM using ^{1}H/^{23}Na NMR

In this section, we focus on three-phase ISSM via measurement on both the ^{1}H and ^{23}Na NMR frequencies. The results are described of a similar coreflooding experiment as in the previous section, but with the saturation profiles acquired at a significantly stronger MRI magnetic field strength. The focus is primarily on the quality of the dual-resonance MRI data, not on the interpretation of the experiment in terms of relative permeability curves.

In addition to the drainage part of the coreflood, (*n*-)decane is injected into the rock at the end of the experiment. In contrast to perfluorinated oil, decane contains hydrogen atoms and is therefore visible on ^{1}H, but still not on ^{23}Na NMR. This serves as an illustration of the ability to distinguish three phases (brine, decane, perfluorinated oil) as in the case of a live crude experiment.

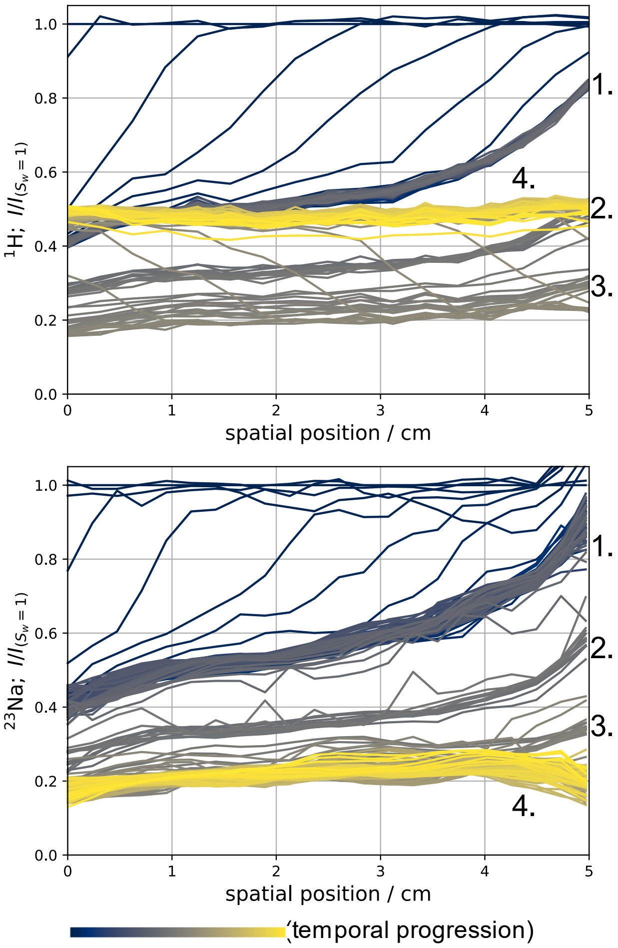

Fig. 7. Saturation profiles acquired using ^{1}H/^{23}Na dual-resonance MRI during unsteady-state drainage coreflood. Profiles acquired on ^{1}H are at the top, ^{23}Na at the bottom. Both sets of profiles are plotted along the same time axis. Flow direction is from left to right. Points 1—3 indicate the end of three successive injection steps with perfluorinated oil at increasing flow rates; point 4 marks the end of the final step, in which decane was injected. These points correspond to times when saturation profiles had stabilised.

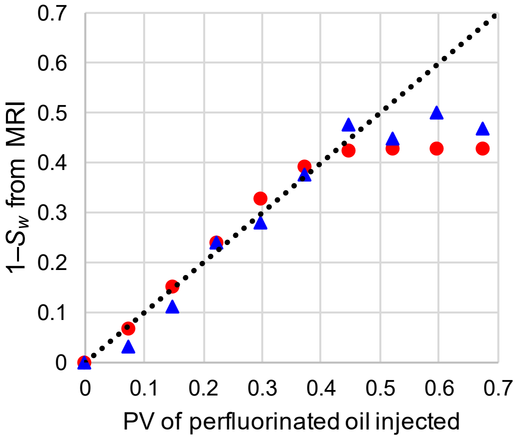

Fig. 8. Comparison of the desaturation seen in the ^{1}H (●) and ^{23}Na (▲) MRI experiment versus the number of pore volumes of perfluorinated oil injected prior to breakthrough of the flood front. For reference, the dotted line is the 1:1 identity.

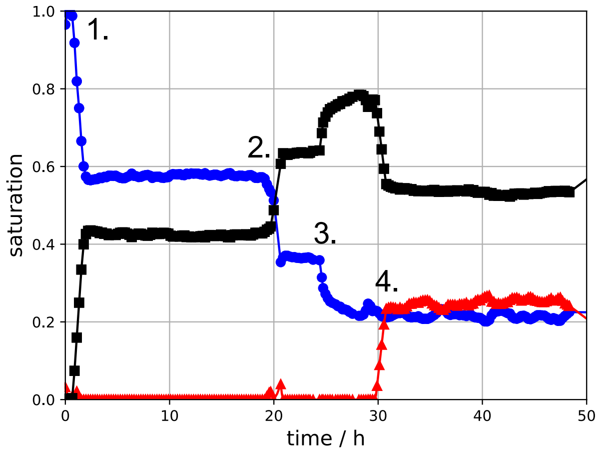

Fig. 9. Comparison of average three-phase saturations across the rock sample as a function of experimental time: brine (S_w, ●), perfluorinated oil (S_g, ■) and decane (S_o, ▲). Time points 1—3 indicate the onset of three successive injection steps with perfluorinated oil at increasing flow rates; point 4 marks the start of the final step, in which decane was injected.

Because of the reasons described in the introduction related to faster signal relaxation at stronger field strengths, quantitative data acquisition at this field is more challenging. At the same time, higher field strengths allow easier observation of less sensitive nuclei such as ^{23}Na.

The saturation profiles measured during the experiment are shown in Fig. 7. The experimental acquisition time for each of the saturation profiles shown was about five minutes, which makes it possible to follow the flood front as it passes through the rock sample. The signal-to-noise ratio of the ^{23}Na profiles is significantly lower than that of the ^{1}H profiles, but they were numerically de-noised using Total Variation filtering in the time domain, which reduces the noise level while preserving edges (such as the flood front).

It is expected that the ^{1}H and ^{23}Na profiles look identical, except for two separate time windows. At the beginning of the experiment, while the flood front is passing through, a slight shift between the ^{23}Na and ^{1}H profiles is expected because the profiles are acquired successively. At the end of the experiment, when decane is injected, it is expected to displace the more mobile perfluorinated oil phase, while leaving the brine in place. This would lead to an increase in amplitude of the ^{1}H profiles, while the amplitude of the ^{23}Na profiles should remain unchanged. These features are indeed observed (Fig. 7).

Fig. 8 shows that, again, the reduction in saturation seen in MRI prior to breakthrough matches the injected pore volume of perfluorinated oil, demonstrating that the measurement is accurate. A comparison of *average* saturation across the sample shows that the ^{1}H and ^{23}Na derived saturations differ to within 3 saturation units prior to injection of decane.

3.2.1 Calculating three-phase saturations

The next step is to calculate three-phase saturations based on the following simple expressions:

$$S_w = \hat{I}[{}^{23}\text{Na}] \tag{1}$$

$$S_o = \left(\hat{I}[\,{}^{1}\text{H}] - \hat{I}[{}^{23}\text{Na}]\right)\frac{HI_w}{HI_o} \tag{2}$$

$$S_g = 1 - S_o - S_w \tag{3}$$

The water saturation S_w is given by $\hat{I}[{}^{23}\text{Na}]$, which is the signal intensity from sodium MRI, normalised to the signal intensity at $S_w = 1$. The oil saturation S_o (i.e., decane) is given by the difference between the normalised signal intensities from sodium and proton MRI, $\hat{I}[\,{}^{1}\text{H}] - \hat{I}[{}^{23}\text{Na}]$, corrected for the difference in hydrogen index (*HI*) between the two liquids, $\frac{HI_w}{HI_o}$. The gas saturation S_g (i.e., the saturation of the invisible phase, in this case perfluorinated oil) is equal to $1 - S_o - S_w$.

Assuming a hydrogen index of 0.93 [38] for the brine and 1.01 for decane (measured), the average saturations for brine, decane and perfluorinated oil were calculated as a function of time (Fig. 9). This was done after interpolating the successive ^{1}H and ^{23}Na measurements onto a common time axis. The results indicate that upon injection of decane, only the perfluorinated oil is displaced, while the water saturation remains unchanged.

After injection of decane, no significant capillary end-effect is seen, and the saturations are almost uniform. This means that at the final fluid saturations ($S_w = 0.24$, $S_g = 0.54$ and $S_o = 0.22$) the effective three-phase relative permeability to decane can be estimated from Darcy's law

$$k_{ro} = \frac{Q_o\,\eta_o\,L}{\Delta P\,k\,A} \tag{4}$$

using the measured pressure drop ΔP during injection of decane at injection rate $Q_o = 0.03$ ml/min, which gives $k_{ro} = 0.06$.

The same approach could be taken if the perfluorinated oil phase had been a gas phase. Additionally, a straightforward extension would be to calculate the three-phase saturations at each spatial position in the saturation profiles over time. While this might introduce some additional noise into the data, it would allow direct visualisation of any capillary end-effects for each phase.

3.3 Experiment C: Two-phase ISSM using ^{1}H NMR in presence of supercritical CO_2

Having established the quantitative nature of ISSM using MRI, we now present a coreflooding experiment performed in the presence of supercritical CO_2 within sandstone reservoir rock. While similar corefloods have been described previously (e.g., [39]), standardised protocols for such studies remain underdeveloped. Controlling gas flow under elevated pressure and temperature conditions poses significant challenges—particularly for supercritical CO_2, because its density is highly sensitive to pressure and temperature variations.

A central question in gas flooding experiments is whether drainage and imbibition can be performed sequentially within the same experimental setup. While this would be ideal, several technical and conceptual challenges complicate such an approach. Practically, managing the injection of multiple fluid types in a live-fluid system is complex. Conceptually, it is well known that gas flooding is often ineffective at reducing water saturation to low levels due to the capillary end-effect and the need to limit injection rates to avoid damaging the sample.

These challenges are exacerbated when using gases or supercritical fluids—such as supercritical CO_2—whose low viscosities relative to brine can lead to flow instabilities and early breakthrough, resulting in limited drainage. If the process is then reversed for imbibition, the brine saturation may become so high that gas trapping is minimal, yielding residual/trapped gas saturations (S_{grw}) close to zero. For CO_2, such outcomes are not representative of realistic CCS scenarios.

An alternative approach involves performing the drainage step outside the coreflooding setup using a centrifuge with model fluids (e.g., air/brine). This method provides a stable displacement process capable of achieving significantly lower water saturations. Following the drainage step, the sample is mounted in the core holder, the model non-wetting phase is replaced with supercritical CO_2, and the imbibition experiment is carried out by displacing the CO_2 with brine. This methodology was adopted in the present study.

Drainage by centrifuge reduced the rock sample to an average brine saturation S_w of 0.35. The sample was then installed in the core holder within the MRI system, and the imbibition coreflood was initiated.

The saturation profiles (Fig. 10) illustrate the progression of the water saturation flood front through the sample prior to breakthrough, followed by a uniform saturation distribution after breakthrough during the injection of the first five pore volumes. The uniformity observed post-breakthrough—indicating the absence of a capillary end-effect—along with the cessation of CO_2 production over several subsequent pore volumes (Fig. 11), confirms that the sample exhibits strongly water-wet behaviour.

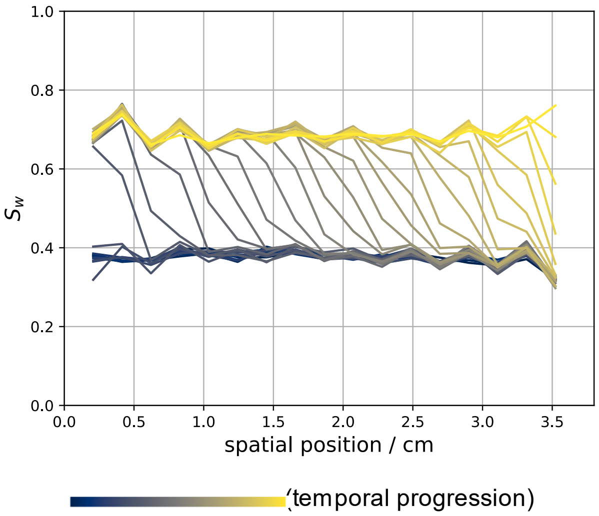

Fig. 10. Unsteady-state imbibition coreflood into a CO_2-saturated reservoir rock sample, initially at an average water saturation (S_w) of 0.35. Shown are saturation profiles (^{1}H) acquired during injection of the first 1.3 pore volumes of brine. Flow is from left to right. Brine was injected at a constant rate of 0.02 ml/min (Darcy velocity: 0.04 mm/min).

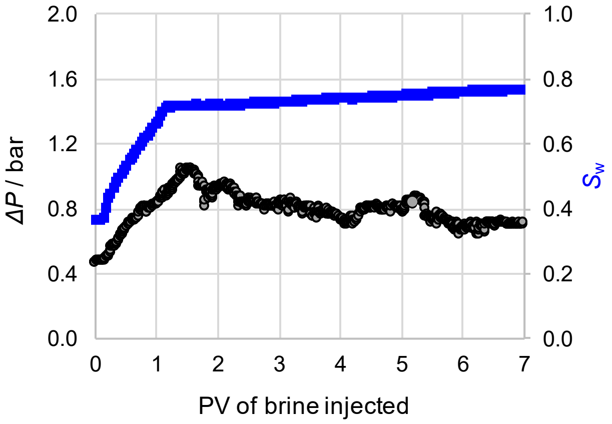

Fig. 11. Unsteady-state imbibition of brine into a CO_2-saturated reservoir rock, initially at S_w = 0.35. Data correspond to the passage of the flood front at a brine injection rate of 0.02 ml/min (as in Fig. 10). Shown are average water saturation (S_w, ■), calculated from MRI-derived saturation profiles, and pressure drop (ΔP, ●) over the first seven injected pore volumes of brine.

As described in [40], the trapped gas saturation (S_{grw}) can be estimated from the average saturation immediately following breakthrough. In this experiment, S_{grw} was determined to be 0.30 ± 0.02. The end-point relative permeability to water at this saturation, calculated using Darcy's law, was $k_{rw} = 0.2$. Consistent with recent findings (see [40] for a detailed discussion), continued brine injection initiates gas dissolution, as evidenced by the gradual increase in S_w after breakthrough. Although there is a slight mismatch between the injected volume (~1.1 PV) and the observed saturation change (0.35 PV) at breakthrough—corresponding to a fluid volume of about 1.8 mL—this is attributed to the inherent difficulty in controlling gas displacement dynamics and is small relative to the internal dead volumes. Nevertheless, the data support quantitative estimation of trapped gas saturations.

4 Conclusions

In this work, it was shown that MRI can be used for quantitative in situ saturation monitoring during coreflooding, and a few approaches were highlighted whereby MRI ISSM can provide inherent multi-phase fluid contrast without a need to use contrast agents. This framework is directly applicable to workflows supporting gas trapping analysis, WAG optimization, and CCS storage efficiency, especially in systems where conventional imaging techniques struggle with phase discrimination.

At low magnetic field, where ^{1}H NMR is feasible and only one of the phases contains protons, quantitative saturation measurements were successfully obtained during an unsteady-state drainage coreflood. This was demonstrated using a perfluorinated oil, effectively simulating CO_2-driven drainage in the context of CCS.

It is important to emphasise that the use of perfluorinated oils in this study is functionally equivalent to the use of gas phases such as CO_2, CH_4, or N_2, which are similarly invisible to ^{1}H and ^{23}Na NMR. The imaging and saturation quantification strategies described here apply equally well to true gas-liquid systems, provided that experimental parameters (e.g., pressure, flow stability, and wetting conditions) are adequately controlled. In this respect, the perfluorinated oil serves as a practical proxy that simplifies experimental design while validating the broader applicability of the method to CCS and EOR processes involving compressible fluids.

To maintain quantitative accuracy in the presence of relaxation-induced signal loss, an offset correction approach was applied to the saturation profiles, and validated through a mass balance cross-check.

Furthermore, the unsteady-state coreflood was interpretable in terms of relative permeability curves by means of numerical simulation and history matching using a minimisation algorithm. This method does not involve calculating gradients from the saturation profiles [15,16], which enhances its robustness to the presence of noise. An additional advantage of the minimisation approach is its ability to provide uncertainty margins on the inferred relative permeability curves. Accurate results depend on assigning appropriate weights to the various datasets—namely injection pressures, produced volumes, and saturation profiles.

At high magnetic field, a more flexible measurement strategy becomes available through dual-resonance NMR, enabling simultaneous detection of ^{1}H and ^{23}Na, with ^{23}Na providing brine-specific contrast. While such hardware configurations are increasingly standard, this study presents a validated method for resolving three-phase saturations in situ—a capability not previously demonstrated in coreflooding. Although the focus here was on establishing the data acquisition framework, future work should extend this to interpretation in terms of full three-phase relative permeability curves. Importantly, the quantitative accuracy of MRI may be reduced at higher field due to faster transverse relaxation caused by susceptibility-induced gradients, particularly in low-permeability rocks with small pores. Nonetheless, further optimisation of pulse sequences and acquisition protocols is expected to mitigate these limitations significantly.

Two related applications are worth highlighting in this context. The first involves single-resonance ^{23}Na MRI for selective brine saturation monitoring; the second applies the same dual-resonance principle to ^{1}H/^{13}C imaging, where ^{13}C replaces ^{23}Na to selectively detect carbon-containing phases such as hydrocarbons or supercritical CO_2. With the existing setup, ^{23}Na MRI can be used independently in two-phase coreflooding experiments to monitor brine saturation, regardless of whether the non-wetting phase contains hydrogen. In a three-phase system, the proposed ^{1}H/^{13}C configuration could enable direct access to individual phase saturations, with ^{13}C capturing the non-aqueous phases containing carbon, and ^{1}H detecting both brine and liquid hydrocarbon components. Despite its inherently lower sensitivity, ^{13}C typically exhibits longer transverse relaxation times than ^{23}Na, owing to its spin-½ property, thereby reducing signal loss in echo-based imaging. The feasibility of this approach has recently been demonstrated under two-phase flow conditions, where ^{13}C-based saturation profiling was successfully implemented [17]; when combined with established ^{1}H imaging, this provides a clear route to three-phase saturation monitoring. This method may be suitable for both steady- and unsteady-state coreflooding, where quasi-steady conditions follow each change in flow rate or fractional flow. Under such conditions, longer acquisition times are permissible, making the ^{1}H/^{13}C configuration feasible. A key requirement for this method is sufficient ^{13}C density contrast between the two carbon-bearing phases—such as liquid and gaseous hydrocarbons, or liquid hydrocarbons and supercritical CO_2—to enable reliable phase discrimination via NMR.

Finally, to illustrate the application of quantitative ISSM in the presence of an actual gas phase, an unsteady-state imbibition coreflood was conducted using a sample initially saturated with supercritical CO_2. This experiment posed significant challenges due to the strong dependence of CO_2 density to fluctuations in pressure and temperature. However, ^{1}H NMR provided inherent contrast between the brine and CO_2 phase, as CO_2 contains no protons and is therefore invisible to ^{1}H NMR. This allows clear visualisation of the advancing flood front and enabled the estimation of trapped gas saturation.

The authors gratefully acknowledge Ian Nicholson of MRF Innovations Ltd (UK) for his construction of the dual-resonance probe used in the ImaCore MRI system; Derrick Green of Green Imaging Technologies Inc. (Canada) for enabling programmable frequency switching; and Steffen Berg of Shell Global Solutions Intl B.V. (The Netherlands) for his valuable insights on inverse modelling.

References

[1] H.J. Welge, J. Pet. Technol. **4**, 91–98 (1952).

[2] E.F. Johnson, D.P. Bossler, V.O. Naumann Bossler, Pet. Trans. **216**, 370–372 (1959).

[3] D.D. Huang, M.M. Honarpour, J. Pet. Sci. Eng. **19**, 103–117 (1998).

[4] R. Gupta, D. Maloney, *Proc. Int. Symp. Soc. Core Analysts*, St John's, Canada, SCA2015-001 (2015).

[5] H.J. Vinegar, S.L. Wellington, Rev. Sci. Instrum. **58**, 96–107 (1987).

[6] B.A. Baldwin, W.S. Yamanashi, Magn. Reson. Imaging **6**, 493–500 (1988).

[7] D. Xiao, B.J. Balcom, J. Magn. Reson. **243**, 114–121 (2014).

[8] S. Chen, F. Qin, K.-H. Kim, A. Watson, *Proc. SPE 67th Annu. Tech. Conf. Exhib.*, Washington, D.C., USA, SPE 24760 (1992).

[9] N.P. Ramskill, I. Bush, A.J. Sederman, M.D. Mantle, M. Benning, B.C. Anger, M. Appel, L.F. Gladden, J. Magn. Reson. **270**, 187–197 (2016).

[10] N.P. Ramskill, I. Bush, A.J. Sederman, M.D. Mantle, L.F. Gladden, *Proc. Int. Symp. Soc. Core Analysts*, St John's, Canada, SCA2015-041 (2015).

[11] A. Brautaset, G. Ersland, A. Graue, J. Stevens, J. Howard, *Proc. Int. Symp. Soc. Core Analysts*, Abu Dhabi, UAE, SCA2008-41 (2008).

[12] M.P. Enwere, J.S. Archer, J. Pet. Sci. Eng. **11**, 73–89 (1994).

[13] J. Siavashi, A. Najafi, M. Sharifi, J. Fahimpour, M. Shabani, B. Liu, K. Liu, J. Yan, M. Ostadhassan, Fuel **308**, 122047 (2022).

[14] R.N. Kulkarni, A.T. Watson, J.-E. Nordtvedt, Magn. Reson. Imaging **16**, 707–709 (1998).

[15] M.S. Zamiri, A. Afrough, F. Marica, L. Romero-Zerón, B. Nicot, B.J. Balcom, Petrophysics **65**, 699–710 (2024).

[16] M.S. Zamiri, N. Ansaribaranghar, F. Marica, A. Ramírez Aguilera, D. Green, C. Caubit, B. Nicot, B.J. Balcom, *Proc. Int. Symp. Soc. Core Analysts*, SCA2024-1032 (2024).

[17] N. Ansaribaranghar, M.S. Zamiri, L. Romero-Zerón, F. Marica, A. Ramírez Aguilera, D. Green, B. Nicot, B.J. Balcom, Petrophysics **66**, 169–182 (2025).

[18] Y. Zhao, Y. Zhang, X. Lei, Y. Zhang, Y. Song, Energy **203**, 220 (2020).

[19] R.N. Kulkarni, A.T. Watson, J.-E. Nordtvedt, A. Brancolini, O. Johnsen, *Proc. SPE European Pet. Conf.*, Milan, Italy, SPE 36855 (1996).

[20] N.P. Ramskill, A.J. Sederman, M.D. Mantle, M. Appel, H. de Jong, L.F. Gladden, Transp. Porous Media **121**, 15–35 (2018).

[21] J. Mitchell, J. Staniland, R. Chassagne, E. Fordham, Transp. Porous Media **94**, 683–706 (2012).

[22] N. Ansaribaranghar, M.S. Zamiri, L. Romero-Zerón, F. Marica, A.R. Aguilera, D. Green, B. Nicot, B.J. Balcom, Petrophysics **66**, 155–168 (2025).

[23] J. Mitchell, E.J. Fordham, Microporous Mesoporous Mater. **269**, 109–112 (2018).

[24] J. Mitchell, J. Pet. Sci. Eng. **146**, 360–368 (2016).

[25] D.P. Green, J. Gardner, B.J. Balcom, M.J. McAloon, P. de J. Cano-Barrita, *Proc. SPE Symp. Improved Oil Recovery*, Tulsa, Oklahoma, USA, SPE 110518 (2008).

[26] D.P. Green, J.R. Dick, M. McAloon, P.F. de J. Cano-Barrita, J. Burger, B.J. Balcom, *Proc. Int. Symp. Soc. Core Analysts*, Abu Dhabi, UAE, SCA2008-01 (2008).

[27] C. Lindsay, C. Cornwall, D. Green, *Proc. Int. Symp. Soc. Core Analysts*, Noordwijk, The Netherlands, SCA2009-20 (2009).

[28] D. Green, D. Veselinovic, B. Balcom, F. Marica, *Proc. Int. Symp. Soc. Core Analysts*, Aberdeen, UK, SCA2012-32 (2012).

[29] C.E. Muir, B.J. Balcom, Magn. Reson. Chem. **51**, 321–327 (2013).

[30] L. Li, H. Han, B.J. Balcom, J. Magn. Reson. **198**, 252–260 (2009).

[31] C. Straley, G. Leu, *Proc. Int. Symp. Soc. Core Analysts*, Trondheim, Norway, SCA2006-31 (2006).

[32] R.L. Kleinberg, M.A. Horsfield, J. Magn. Reson. **88**, 9–19 (1990).

[33] S. Krevor, M.J. Blunt, S.M. Benson, C.H. Pentland, C. Reynolds, A. Al-Menhali, B. Niu, Int. J. Greenh. Gas Control **40**, 221–237 (2015).

[34] S. Berg, H. Dijk, E. Unsal, R. Hofmann, B. Zhao, V.R. Ahuja, Comput. Geotech. **168**, 106091 (2024).

[35] F. Lomeland, E. Ebeltoft, W.H. Thomas, *Proc. Int. Symp. Soc. Core Analysts*, Toronto, Canada, SCA2005-32 (2005).

[36] S.M. Skjæveland, L.M. Siqveland, A. Kjosavik, W.L.H. Thomas, G. Virnovsky, SPE Res Eval & Eng. **3**, 60–67 (2000).

[37] A. Fadili, S. Berg, *Proc. Int. Symp. Soc. Core Analysts*, Hannover, Germany, SCA2025-1012 (2025).

[38] S.A. Hertel, B.C. Anger, K. Smith, M. Appel, *Proc. Int. Symp. Soc. Core Analysts*, Snowmass, Colorado, USA, SCA2016-042 (2016).

[39] S. Berg, S. Oedai, H. Ott, Int. J. Greenh. Gas Control **12**, 478–492 (2013).

[40] Y. Gao, T. Sorop, N. Brussee, H. van der Linde, A. Coorn, M. Appel, S. Berg, Petrophysics **64**, 368–383 (2023).